


Article

Determination of the Physical Parameters of AGNs in Seyfert 1 Galaxies LEDA 3095839 and VII Zw 244 Based on Spectropolarimetric Observations

Accepted for publication in Universe

Elena Shablovinskaya ¹, Mikhail Piotrovich ^{1,2,*} , Eugene Malygin ¹, Stanislava Buliga ^{1,2} and Tinatin Natsvlshvili ²

¹ Special Astrophysical Observatory RAS, 369167 Nizhnii Arkhyz, Russia; e.shablie@yandex.com (E.S.); male@sao.ru (E.M.); aynim@yandex.ru (S.B.)

² Central Astronomical Observatory at Pulkovo RAS, 196140 Saint-Petersburg, Russia; tinatingao@mail.ru

* Correspondence: mpiotrovich@mail.ru

Abstract: Here we present the detailed investigation of AGNs in two Seyfert 1 galaxies, LEDA 3095839 and VII Zw 244. Both of them were observed within the photometric reverberation mapping project in Special Astrophysical Observatory of the Russian Academy of Sciences (SAO RAS), during which we earlier obtained the SMBHs masses. After that, both galaxies were observed in spectropolarimetric and polarimetric modes on the BTA 6 m telescope of the SAO RAS with the focal reducer SCORPIO-2. The linear polarization of the continuum and broad Balmer lines has been measured. It was found that (i) there were no signs of equatorial scattering in the LEDA 3095839 galaxy in the broad H α line, and we were able to estimate the value of SMBH spin and the magnetic field strength in the disk from the level of continuum polarization; (ii) for the galaxy VII Zw 244, the presence of equatorial scattering was shown, due to which the mass of the SMBH was independently measured, the inclination angle of the system was obtained, and the value of the spin was estimated.

Keywords: accretion disks; magnetic fields; polarization; active galactic nuclei; supermassive black holes



Citation: Shablovinskaya, E.; Piotrovich, M.; Malygin, E.; Buliga, S.; Natsvlshvili, T. Determination of the Physical Parameters of AGNs in Seyfert 1 Galaxies LEDA 3095839 and VII Zw 244 Based on Spectropolarimetric Observations. *Universe* **2022**, *1*, 0. <https://doi.org/>

Academic Editor:

Received: 15 June 2022

Accepted: 15 July 2022

Published:

Publisher's Note: MDPI stays neutral with regard to jurisdictional claims in published maps and institutional affiliations.



Copyright: © 2022 by the authors. Licensee MDPI, Basel, Switzerland. This article is an open access article distributed under the terms and conditions of the Creative Commons Attribution (CC BY) license (<https://creativecommons.org/licenses/by/4.0/>).

1. Introduction

Active galactic nuclei (AGN), as the most powerful sources in the Universe, are unique objects where the physical state of the matter in extreme conditions can be tested. As AGN radiation is produced due to the accretion of matter on the supermassive black holes (SMBH) in the center of host galaxies, the determination of such basic SMBH parameters as spin (dimensionless angular momentum) and mass is a crucial issue of modern astrophysics. Moreover, measuring these parameters is an important task, because it allows us to trace the evolution of SMBH correlated with the evolution of galaxies at different cosmological epochs [1,2].

As for SMBH spin $a = cJ/(GM_{\text{BH}}^2)$ (where J is the angular momentum, M_{BH} is the mass of the black hole, G is the gravitational constant and c is the speed of light), it is believed that the spin plays a central role in the generation of relativistic jets in AGN, and the power of the relativistic jet is often used to determine the spin of the SMBH [3]. It is believed that jets are formed due to the presence of a magnetic field in the disk. The kinetic power of a relativistic jet can be obtained by estimating the magnetic field near the SMBH event horizon using several jet generation mechanisms: Blandford–Znajek mechanism [4], Blandford–Payne mechanism [5] and Garofalo mechanism [6].

Radiative efficiency $\varepsilon = L_{\text{bol}}/(\dot{M}c^2)$ (where L_{bol} is the bolometric luminosity of AGN and \dot{M} is the accretion rate) depends significantly on the spin [7–10]. So we could obtain the spin value by estimating the radiative efficiency.

The polarimetric observations of AGNs show polarization in different ranges [11–19]. Spectropolarimetric characteristics of the accretion disk can demonstrate the effect of the presence of the magnetic field. Several mechanisms have been proposed for the occurrence of polarization in different structures (relativistic jets, the plane or warped accretion disks, toroidal rings near the accretion disks), such as the light scattering in accretion disks or synchrotron radiation. There are several models of accretion disks (see for example Pariev et al. [20]). The most popular and simple model for our objects (Seyfert 1 AGNs with $0.01 < l_E < 0.3$ [21], where $l_E = L_{\text{bol}}/L_{\text{Edd}}$ is Eddington ratio and L_{Edd} is Eddington luminosity) is the optically thick, geometrically thin Shakura–Sunyaev disk [22].

The methods for determining masses of astrophysical objects are commonly based on the measurement of the matter rotating around. In the case of SMBH, there are several direct and indirect approaches (see [23] for a review), and reverberation mapping is one of the most reliable direct methods used for low-redshift type 1 quasars [24]. The method is based on the estimation of the time delay between the continuum radiation of the accretion disk and the radiation in the broad emission lines produced in the BLR (broad-line region), which is why it requires a long observational time series. This raises an issue of measuring SMBH masses from a single-epoch observed spectrum of quasars by calibration relations which is still under development [23].

Afanasiev and Popović [25] suggested a new alternative approach to trace the gas velocities in BLR in equatorially scattered type 1 AGN using single-epoch spectropolarimetric data. The method is based on measuring the variation of the polarization angle as a function of BLR gas velocity upon the radiation of the differently rotating BLR disk reflects from the inner boundary of the dusty torus. A detailed description is given further in Section 3.2.2 This method is still applied to a relatively small number of close Seyfert 1 galaxies (~ 30 AGN) (see [26,27]), yet it revealed the statistically approved and stable results of SMBH measurements. Moreover, in the same work it was shown that comparison between two independent SMBH mass measurements given by the spectropolarimetric and reverberation mapping approaches allows one to estimate the inclination angle of the AGN relative to the observer.

Therefore, as it was described above, the polarimetric tools provide us with valuable information about the structure and physical parameters of geometrically unresolved central parts of AGN. This allows us to take a more detailed look at the physical characteristics of SMBH and gas around in individual AGNs to build more general models of the galaxy's evolution. For a thorough analysis of the physical parameters previously (see [26]) for conducting spectropolarimetric observations on the 6 m BTA telescope and searching for signs of equatorial scattering, the main attention was paid to the sample of AGNs with SMBH masses measured by reverberation mapping approach (e.g., [28]). Within this work we decided to focus our attention on the AGNs examined earlier by our group in the Special Astrophysical Observatory of the Russian Academy of Sciences (SAO RAS) using the photometric reverberation mapping [29]. Currently, there are two type 1 AGN from that sample—LEDA 3095839 and VII Zw 244, where we have estimated the BLR size R_{BLR} and, consequently, the SMBH masses (or so-called virial products, see Section 3.1.3) [30]. It motivated us to select these objects for further investigation. The polarimetric observations revealed the non-zero level of the polarization in spectra of both galaxies, yet a further detailed examination showed the diverse origin of the observed effects.

The paper is organized as follows. In Section 2 we describe the polarimetric observations and data reduction procedures. The results of the data analysis are provided in Section 3, where for the objects the continuum or broad line polarization is estimated, and bolometric

luminosity, inclination angle, spin, and magnetic field strength are calculated. The conclusions are given in Section 4.

2. Observations and Reduction

The observations were carried out with the 6-meter BTA telescope of the SAO RAS. We used a modified SCORPIO-2 spectrograph [31] in spectropolarimetric and polarimetric modes. The observation log is presented in Table 1, which shows the object names, redshift z , observational mode, volume phase holographic grism (VPHG, for spectropolarimetry) or medium-band filter from SED-set¹ (for polarimetry), date of observations, exposure time, the direct image quality (seeing), air mass, and position angle (PA). For both polarimetry and spectropolarimetry we use a double Wollaston prism [32,33] as a polarization analyzer, that allows one to simultaneously obtain four images corresponding to the electric-vector oscillation directions of 0° , 90° , 45° , and 135° and, consequently, three Stokes parameters I , Q , and U within one exposure.

It is important to note that on 18 November 2019, during polarimetric observations of LEDA 3095839, the zenith distance of the Moon illuminated by 60% was $\sim 38^\circ$. On 12 October 2020, during the spectropolarimetric observations of VII Zw 244, the Moon, illuminated by 19%, rose to a zenith distance of 74° . At the same time, the obtained polarization values coincided with the measurements of the same objects observed on moonless nights.

Table 1. Log of BTA observations of studied AGN.

Object	z	Mode	VPHG /Filter	Date dd/mm/yy	Exposure, s	Seeing	Air Mass	PA, Degrees
LEDA 3095839	0.109	specpol	1026@735	3 March 20	$300 + 9 \times 600$	1".7	1.4	106.3
		pol	SED700 SED725	18 November 2019	$60 + 4 \times 80$ $60 + 4 \times 50$	1".3	1.2	55.6
VII Zw 244	0.131	specpol	940@600	12 October 2020	6×900	1".6	1.3	0.0
		pol	SED700 SED725 SED750	7 November 2019	7×180 7×180 7×180	2".5	1.3	54.2

2.1. Spectropolarimetry

In the spectropolarimetric mode, the slit length is $1'$. In the case of observations of both AGNs, the slit width was $\sim 2''$. The spectral resolution is determined by the slit width and the used spectral grating². Spectropolarimetric data for LEDA 3095839 was obtained on March 3, 2020 with the total exposure of ~ 1.6 h. The VPHG1026@735 grism with the CCD detector E2V 42-90 (with a pixel size of $13.5 \times 13.5 \mu\text{m}$; in spectral mode with binning 2×1 , giving a frame of size $\sim 2 \text{ k} \times 2 \text{ k px}$ and scale $0''.352 \times 0''.176$ per pixel²) provided the spectrum coverage of $5800\text{--}9500\text{\AA}$ with the FWHM $\sim 10\text{\AA}$. In this configuration, a blocking GS-17 filter was also used for object LEDA 3095839 to suppress the grating second order. We also note that for LEDA 3095839, we do not provide here the red part of the spectrum beyond 8200\AA due to the presence of "fringes" for CCD E2V 42-90, which leads to large noise upon subtracting the sky background. The BTA prime focus adapter was used to calibrate the spectrum [34]. For this, we obtained the comparison spectrum from a He-Ne-Ar lamp and flat field frames. An extremely important calibration of the three-dot mask (three-dot test) was also

obtained, which makes it possible to take into account the geometric distortions of the field in received frames, which is critical for the analysis of the polarization of such faint objects as AGNs.

Spectropolarimetric data for VII Zw 244 was obtained on 12 October 2020. The total exposure was 1.5 h. VPHG940@600 with 2''-wide slit, with LP425 filter (for second order cutoff) together with CCD E2V 261-84 (with pixel size $15 \times 15 \mu\text{m}$; in spectral mode with 2×4 binning, giving a frame size of $\sim 2 \text{ k} \times 520 \text{ px}$ and scale $0''.391 \times 0''.782$ per pixel² [35]) provided the spectrum coverage of 3500–8500 Å with FWHM $\sim 12 \text{ \AA}$. The comparison spectrum, three-dot test, and flat fields were also taken with the prime focus adapter. Observations of objects were accompanied by observations of polarized standard stars and stars with zero polarization.

Introducing the instrumental parameters K_Q and K_U , which characterize the transmission of polarization channels, determined from observations of unpolarized standard stars, as well as $I_0(\lambda)$, $I_{45}(\lambda)$, $I_{90}(\lambda)$, and $I_{135}(\lambda)$ as the intensity at four polarization directions, we can measure three Stokes parameters:

$$I(\lambda) = I_0(\lambda) + I_{90}(\lambda)K_Q(\lambda) + I_{45}(\lambda) + I_{135}(\lambda)K_U(\lambda) \quad (1)$$

$$Q(\lambda) = \frac{I_0(\lambda) - I_{90}(\lambda)K_Q(\lambda)}{I_0(\lambda) + I_{90}(\lambda)K_Q(\lambda)} \quad (2)$$

$$U(\lambda) = \frac{I_{45}(\lambda) - I_{135}(\lambda)K_U(\lambda)}{I_{45}(\lambda) + I_{135}(\lambda)K_U(\lambda)} \quad (3)$$

Here and below we use Q and U to denote the normalized Stokes parameters.

Then, by determining the zero-point of the polarization angle φ_0 from observations of polarized standard stars, one can determine the degree of linear polarization $P(\lambda)$ and the polarization angle $\varphi(\lambda)$ as:

$$P(\lambda) = \sqrt{Q^2(\lambda) + U^2(\lambda)} \quad (4)$$

$$\varphi(\lambda) = \frac{1}{2} \arctan\left[\frac{U(\lambda)}{Q(\lambda)}\right] + \varphi_0 \quad (5)$$

The observation technique and data reduction are described in more detail in [36]. Interstellar medium (ISM) polarization and atmospheric depolarization were taken into account using polarimetric measurements of field stars around the studied AGN.

2.2. Polarimetry

In the polarimetric mode with double Wollaston prism for LEDA 3095839, we obtained 5 frames each with ~ 1 minute exposure time in interference SED filters with bandwidths of the order of $\sim 250 \text{ \AA}$ with 2×2 binned (frame size $1 \text{ k} \times 1 \text{ k px}$ and scale $0''.352 \times 0''.352$ per pixel) CCD E2V 42-90. One filter is oriented to the $\text{H}\alpha$ emission line, and the second one is oriented to the continuum near. For VII Zw 244, we obtained polarimetric data using the same CCD with the same binning in three filters (one covers the $\text{H}\alpha$ line, and two cover the continuum around), 7 frames each with ~ 3 min exposure time. In case of observations of both objects in the image polarimetry mode, the double Wollaston prism produces four images of the entrance pupil bounded by a rectangular mask, so each image has a field of view of $\sim 6' \times 1'$.

It is important to clarify that in both cases we oriented the instrument so that the masked field contained bright non-variable stars (at a distance of $1'.6$ from LEDA 3095839 and at a distance of $4'.6$ from VII Zw 244). This allows the use of a differential polarimetry technique that minimizes the effects of the depolarization due to the atmospheric variations that can reach up to 2–3% [36] and instrumental errors mostly due to the prism transmission which is

about 0.2% according to the independent measurements of the polarized standard stars [26]. To find more about differential polarimetry see [37]. This technique ensured an accuracy of polarimetry of about $\sim 0.1\%$ for the field stars. Within this work, obtaining AGN polarimetry data in filters allows us to refine the average polarization value in objects and roughly estimate the effect of ISM polarization.

Since the type 1 AGN linear polarization is usually close to zero, as it was shown in [38], when calculated by Equation (4), the degree of polarization P turns out to be biased. So, for spectropolarimetric observations, we used the following relation to obtain the unbiased value of the polarization degree:

$$P_{\text{unbiased}} = P \cdot \sqrt{1 - (K \cdot \sigma_P / P)^2}, \quad (6)$$

where P is measured degree of fractional linear polarization, σ_P is the corresponding error obtained from observational data as the standard deviation, $\sqrt{1 - (K \cdot \sigma_P / P)^2}$ is called a Rice factor. Simmons and Stewart [38] recommended the bias correction factor $K = 1.41$ for low signal-to-noise ratios ($\sigma_P / P \lesssim 0.7$) based on the maximum likelihood estimator of the true value of the polarization degree. Note that we do not correct the measured polarization values obtained using image polarimetry, because the measured accuracy is an order of magnitude higher than the accuracy of spectropolarimetric measurements.

3. Results

3.1. Object LEDA 3095839

3.1.1. Continuum Polarization

The results of LEDA 3095839 spectropolarimetry are shown in Figure 1. The spectrum is given in the 6500–8200 Å wavelength range, where the shifted broad H α line is located.

The first panel in Figure 1 shows the integral spectrum in ADU units, not corrected for the device sensitivity curve. Note that the atmospheric absorption bands of molecular oxygen B-band (6860–6917 Å) and A-band (7590–7720 Å) are visible in the continuum spectrum of the object; in addition, in the range ~ 7150 –7350 Å there is a water vapor absorption band, which appears exactly in H α broad line. On panel 1 and others, the H α line center and the [NII] narrow lines are marked.

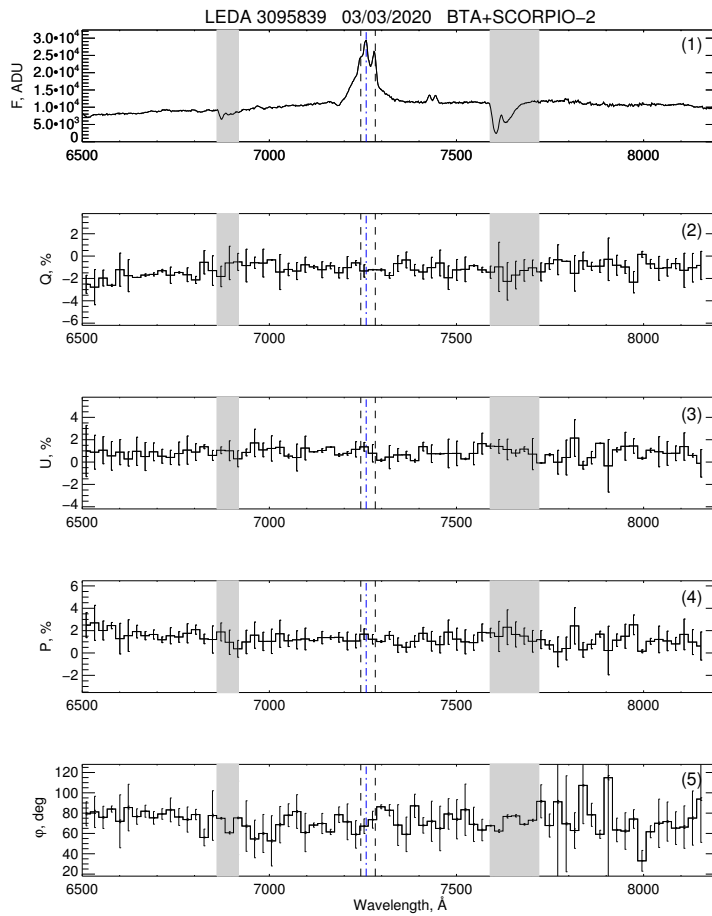


Figure 1. Spectropolarimetric data for LEDA 3095839 in the range of 6500–8200 Å. From the top to the bottom: integral spectrum in ADU F (1), normalized Stokes parameters Q (2) and U (3), polarization degree P (4), and polarization angle φ (5). The vertical blue dash-dot line denote the position of $H\alpha$ line; the vertical black dash lines denote the position of narrow [NII] lines. The atmospheric absorption bands are noted with light grey stripes.

The second and third panels in Figure 1 show the Stokes parameters Q and U binned over the 22 Å-window, corrected for the Wollaston prism transmission and not corrected for the rotation angle of the device. The step of the spectral bin was chosen so that, while estimating the robust average of the measured values over the spectral range and all taken exposures, the outlier points (mostly due to the cosmic ray hints) were corrected. The errors given on the plots are equal to the 1σ level, where σ is the robust standard deviation. Here for the analysis we use the basic robust estimation using 2σ rejection threshold. More details about the algorithm can be found in [39] and references therein. It can be seen that within the broad $H\alpha$ line, there are no significant changes in the Q and U parameters along wavelength, and their variations do not exceed the measurement error. This is the main marker of the absence of the equatorial scattering in the object. Thus, the average value of the Stokes parameters over the observed spectrum is $\langle Q \rangle = -(1.2 \pm 0.4)\%$ and $\langle U \rangle = (0.8 \pm 0.4)\%$. These values coincided with the averaged values from the observations in the polarimetric mode in the medium-band filters on another night: $Q_f = -(1.0 \pm 0.1)\%$ and $U_f = (0.8 \pm 0.2)\%$, which indicates the stability of the object's polarization state on the timeline of observations.

Polarization degree P (panel 4 in Figure 1) also shows no deviations in the $H\alpha$ line from the mean value of the continuum polarization. At the same time, it can be seen that the polarization

level of the object is non-zero, does not change along the wavelength within the error and, upon robust averaging over the entire observed spectrum (which is almost equal to the median value of P), is $\langle P \rangle = (1.3 \pm 0.4)\%$. Polarization angle φ (panel 5 in Figure 1) also does not demonstrate dependence on the wavelength and, in particular, features along the broad line. So, it can also be considered constant within the error with a robust average value of $\langle \varphi \rangle = (73 \pm 8)^\circ$. Note that the presented polarization angle φ is given in instrumental units that are not rotated to the north direction on the celestial plane. The obtained estimates also coincide with the polarization estimates in the filters: $P_f = (1.3 \pm 0.2)\%$ and $\varphi_f = (71 \pm 4)^\circ$.

Since the galactic latitude of the object is $b \sim +33^\circ$, it is worth assuming that the observed polarization is partially or completely influenced by ISM polarization together with depolarization in the atmosphere and the influence of residual instrumental effects. Observations in filters in the polarimetry mode showed that the object's environment is weakly polarized, however, the average polarization value of the neighboring three stars in the field is determined with a large error and is $P_{\text{stars}} \sim (2 \pm 1)\%$ and $\varphi_{\text{stars}} \sim (80 \pm 15)^\circ$. This shows that a significant part of the observed polarization level in the object does not relate to the nature of the source. However, if one tries to correct the additional polarization by the star closest to the object³, then even in this case, the minimum possible intrinsic polarization of the object is $P \sim 0.5\%$. So far, it appears that the observed continuum polarization of the source cannot be totally caused by ISM polarization. It is also important to mention that in the given case in Figure 1 the values of P are presented biased because they could not be properly corrected due to the field polarization providing non-zero Q and U Stokes parameters.

Since we have not found any signs of equatorial scattering in LEDA 3095839 spectra, we further assume that the observed polarization related to the source is generated in the accretion disk. Due to the large error in determining the correction for ISM polarization, we believe that the continuum polarization level in the object is between 0.5% and 1.3%. Thus, further, to determine the physical parameters of AGN, we assume for LEDA 3095839 $P = (0.9 \pm 0.4)\%$. However, it is worth mentioning that if the object intrinsic polarization is higher, up to 1.3%, then it is worth assuming not only polarization mechanisms in the accretion disk, but the complex influence of polarized radiation from different AGN structures, e.g., synchrotron radiation of a jet. Within the framework of this paper, we neglect the influence of other polarization mechanisms.

3.1.2. Bolometric Luminosity

According to Xu and Cao [41], the bolometric luminosity of LEDA 3095839 is $\log [L_{\text{bol}}(\text{erg/s})] = 45.05$. They derive this value from luminosity in B filter $\log [L_B(\text{erg/s})] = 44.39$ using bolometric correction [42]. Our observations on the 6 m BTA telescope give a luminosity value at 5100\AA $\log [L_{5100}(\text{erg/s})] = 43.94$ [30]. There is a serious problem in defining the bolometric correction factors that are used for obtaining luminosity value at a certain wavelength from bolometric luminosity. In the literature, we can find factors that differ 2–3 times [43–47]. In this work we decided to use bolometric correction for luminosity at 5100\AA from Richards et al. [43]: $L_{5100} = L_{\text{bol}}/10.3$. Thus we get the value $\log [L_{\text{bol}}(\text{erg/s})] = 44.95$.

3.1.3. Inclination Angle and Spin Value

To determine the spin value a we need to obtain radiative efficiency ε which depends significantly on the spin [7–10]. Then we could determine spin numerically using the relation [7]:

$$\varepsilon(a) = 1 - \frac{R_{\text{ISCO}}^{3/2} - 2R_{\text{ISCO}}^{1/2} + |a|}{R_{\text{ISCO}}^{3/4} (R_{\text{ISCO}}^{3/2} - 3R_{\text{ISCO}}^{1/2} + 2|a|)^{1/2}} \quad (7)$$

Table 2. Results of our calculations of masses M_{BH} and spins a for our objects. P is polarization degree in [%], $FWHM$ is full width at half maximum of $H\beta$ line in km/s, L_{bol} is bolometric luminosity in erg/s, l_E is Eddington ratio, i is inclination angle in degrees, ϵ is radiative efficiency, B_{H} and B_{H}^* are magnetic field strength at event horizon in Gauss obtained from spectral characteristics and from polarization data respectively, s is the exponent of the power-law dependence of the magnetic field on the radius. For VII Zw 244, the SMBH mass and inclination angle estimations obtained by spectropolarimetry are marked with † symbol.

Object	P	$FWHM$	$\log(L_{\text{bol}})$	l_E	i	$\log(M_{\text{BH}}/M_\odot)$	ϵ	a	$\log(B_{\text{H}})$	$\log(B_{\text{H}}^*)$	s
LEDA 3095839	0.9 ± 0.4	3775	44.95	$0.11^{+0.09}_{-0.05}$	35	$7.881^{+0.153}_{-0.171}$	$0.21^{+0.09}_{-0.07}$	$0.966^{+0.030}_{-0.106}$	$4.06^{+0.24}_{-0.24}$	$3.53^{+0.26}_{-0.53}$	1.77 ± 0.18
				$0.22^{+0.18}_{-0.09}$	45	$7.699^{+0.153}_{-0.171}$	$0.11^{+0.10}_{-0.04}$	$0.736^{+0.226}_{-0.368}$	$4.00^{+0.56}_{-0.34}$	$4.08^{+0.30}_{-1.08}$	1.63 ± 0.23
VII Zw 244	1.4 ± 0.6	3219	45.24	$0.11^{+0.03}_{-0.02}$	18	$8.069^{+0.068}_{-0.075}$	$0.30^{+0.02}_{-0.06}$	$0.996^{+0.002}_{-0.012}$	$4.29^{+0.10}_{-0.13}$	–	–
					$14.3 \pm 3.6^\dagger$	$8.29 \pm 0.30^\dagger$	–	–	–	–	–

where R_{ISCO} is the radius of the innermost stable circular orbit of a black hole and

$$\begin{aligned} R_{\text{ISCO}}(a) &= 3 + Z_2 \pm [(3 - Z_1)(3 + Z_1 + 2Z_2)]^{1/2} \\ Z_1 &= 1 + (1 - a^2)^{1/3}[(1 + a)^{1/3} + (1 - a)^{1/3}] \\ Z_2 &= (3a^2 + Z_1^2)^{1/2} \end{aligned} \quad (8)$$

Here the sign “-” is used for prograde ($a \geq 0$), and the sign “+” for retrograde rotation ($a < 0$).

There are several models connecting the radiative efficiency with such parameters of AGN as mass of SMBH M_{BH} , angle between the line of sight and the axis of the accretion disk i and bolometric luminosity L_{bol} [48–52]. Based on the results of our previous work [53] we decide to use theoretical model developed for Shakura–Sunyaev accretion disk case from Du et al. [50]:

$$\epsilon(a) = 0.105 \left(\frac{L_{\text{bol}}}{10^{46} \text{erg/s}} \right) \left(\frac{L_{5100}}{10^{45} \text{erg/s}} \right)^{-1.5} M_8 \mu^{1.5} \quad (9)$$

Here $M_8 = M_{\text{BH}} / (10^8 M_\odot)$, $\mu = \cos(i)$ and i is the inclination angle between the line of sight and the axis of the disk.

We used the SMBH mass value from Malygin et al. [30] calculated for $f = 1$, where f is the dimensionless parameter characterizing the object geometry and orientation that is usually introduced as following (see [23]):

$$M_{\text{BH}} = f \times (R_{\text{BLR}} \vartheta_{\text{line}}^2 G^{-1}) = f \times V.P., \quad (10)$$

where ϑ_{line} is the velocity of the line-emitting gas in the BLR, G is the gravitational constant, and $V.P.$ is a virial product, which characterizes the least possible value of the M_{BH} as $f \geq 1$ ($f \approx 1 / [\sin^2(i)]$) due to the projection of the gas velocity ϑ_{line} to the line of sight). So far, we assumed that polarized radiation from this object is produced by accretion disk. Thus, based on our polarimetric data [$P = (0.9 \pm 0.4)\%$] and Sobolev–Chandrasekhar mechanism [54–56] with addition of Faraday depolarization from magnetic field [57] we concluded that inclination angle must satisfy the condition $35^\circ \lesssim i \lesssim 55^\circ$. Next, we considered three options: $i = 35^\circ$, $i = 45^\circ$, and $i = 55^\circ$. Table 2 shows results of our calculations for first two options. The results are quite typical for objects of this type [53]. Results for $i = 55^\circ$ are inconclusive and do not allow to determine the value of spin, so we decided not to consider this option further.

3.1.4. Magnetic Field

We were unable to find information about the radio properties of the LEDA 3095839 object in the literature. So we operated on the assumption that it is radio loud and has a jet. Thus, we can estimate the magnetic field strength using the approach from Piotrovich et al. [58]:

$$B_H = \frac{10^{(5.78 \pm 0.07)} \eta \sqrt{\varepsilon}}{l_E^{(0.295 \pm 0.020)} |a| [\cos(i)]^{3/4}} \left(\frac{10^3 \text{ km/s}}{FWHM} \right)^3 \text{ G} \quad (11)$$

Here η is the coefficient depending on the model of relativistic jet generation (in this case $\eta = 1.05^{-0.5}$ [58]) and $FWHM$ is full width at half maximum of spectral line $H\beta$. We use the Eddington ratio $l_E = L_{\text{bol}}/L_{\text{Edd}}$, where $L_{\text{Edd}} = 1.5 \times 10^{38} M_{\text{BH}}/M_{\odot}$ is the Eddington luminosity. For this object we take value $\vartheta_{\text{line}} = 1.5 \times 10^3$ km/s from Malygin et al. [30] and calculate $FWHM = 2.335 k^{-0.5} \vartheta_{\text{line}}$. Here $k \approx 0.88$ is the coefficient arising from the fact that in Malygin et al. [30] ϑ_{line} for this object referred to $H\alpha$ line [29].

Additionally, we use the different approach from Piotrovich et al. [57] that relates the geometry of the magnetic field in an accretion disk to the polarization of its radiation. So we can estimate the magnetic field strength at the event horizon of SMBH B_H^* and the exponent s of the power-law dependence of the magnetic field on the radius $B^*(R) = B_H^*(R_H/R)^s$, where $R_H = GM_{\text{BH}}(1 + \sqrt{1 - a^2})/c^2$ is the radius of the event horizon.

The results of both methods are shown in Table 2. Obtained values of the magnetic field are sufficiently close and quite typical for objects of this type [57,59]. A relatively large error in determining the magnetic field is associated with significant errors in the measurement of the spin value and relatively small polarization degree.

3.2. Object VII Zw 244

3.2.1. Polarization in Broad Lines

The results of AGN VII Zw 244 spectropolarimetry are shown in Figure 2. The spectrum is given in the wavelength range 4500–8000 Å and contains shifted broad lines $H\alpha$, $H\beta$, and $H\gamma$. The panels on Figure 2 correspond to the panels on Figure 1, so the details will be omitted here. The atmospheric absorption bands of molecular oxygen B-band, A-band, and the molecular oxygen emission line 5577 Å are marked on the spectra.

The second and third panels on Figure 2 show the Stokes parameters Q and U binned over the 32 Å-window, corrected for the Wollaston prism transmission and not corrected for the rotation angle of the device. The degree P and the polarization angle φ are binned in the same window. Here the observed values of P not corrected to the bias are presented.

In the entire observed range, the Stokes parameters Q and U show both a slight smooth dependence on the wavelength (mostly in the case of U), and the dramatic variations within the broad lines, where opposite variation patterns could be detected in Q and U parameters. It is important to note that the pattern of the parameter changes in the two lines $H\alpha$ and $H\beta$ repeats each other up to noise; in the $H\gamma$ line, the effect is too small and does not exceed noise, which is why further analysis of polarization is not carried out in this line. It is clearly seen that the degree of polarization of P in broad lines differs significantly (by ~1–1.5%) from the continuum value, and the angle acquires an S-shaped profile with an amplitude significantly exceeding the measurement error. These features indicate the presence of equatorial scattering in the central regions of the AGN [60].

Since the further analysis of the polarized spectrum of the object will concern only the profiles of two broad lines, Figure 3 presents spectral data $H\alpha$ and $H\beta$, recalculated in the velocity range from –14,000 to 14,000 km/s relative to the centers of the lines. Panels 1 and 5 demonstrate the flux F and the polarized flux $F \cdot P$ in counts; the Stokes parameters Q and U (panels 2 and 3) are corrected for the polarization of the field stars calculated from

the polarimetry data in the filters (the correction is equal to 3.1% for Q and -1.8% for U). The polarization degree P and angle φ are recalculated from the Stokes parameters Q and U , taking into account the bias correction (the Rice factor is about 0.67). For the larger visibility the parameters Q , U , P and φ are binned in the window 18 \AA ; the spectrum F is given with 2 \AA resolution, the polarized spectrum $F \cdot P$ —with 6 \AA resolution.

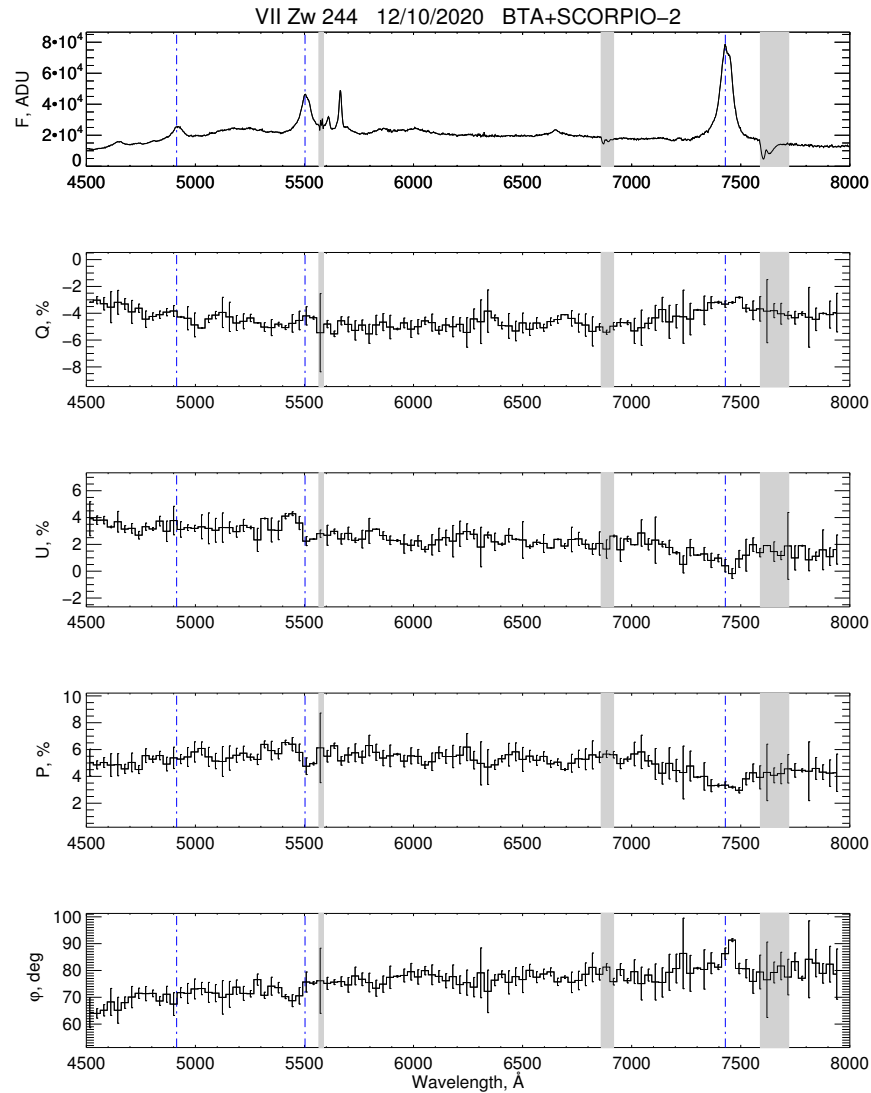


Figure 2. Spectropolarimetric data for VII Zw 244 in the range of 4500–8000 Å. From the top to the bottom: integral spectrum in ADU F (1), normalized Stokes parameters Q (2) and U (3), polarization degree P (4), and polarization angle φ (5). The vertical blue dash-dot line denote the position of (from the left to the right) $H\gamma$, $H\beta$, and $H\alpha$ lines. The atmospheric absorption/emission bands are noted with light grey stripes.

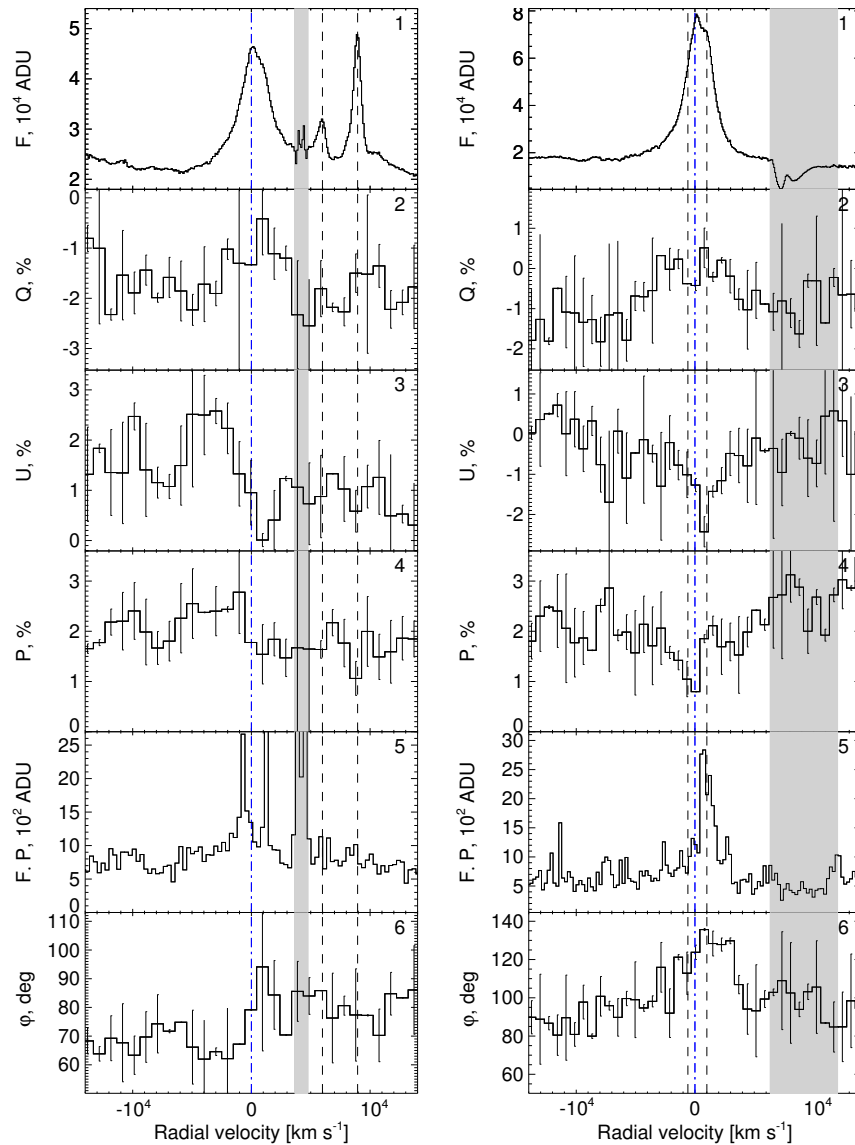


Figure 3. The profiles of $H\beta$ (left) and $H\alpha$ (right) lines. From top to bottom: the intensity in the natural light, the Q and U Stokes parameters, the polarization degree, the polarized flux, and the polarization angle. Note here that the polarization degree is debiased according to the Equation (6). The values on panels 1 and 5 are binned in the 6 \AA window and the values on panels 2–4 and 6—in the 18 \AA window. The black vertical dashed lines mark the narrow lines coming from the NLR—[OIII] lines at $H\beta$ profile and [NII] lines at $H\alpha$ profile. The blue vertical dashed line marks the position of zero velocity. The atmospheric absorption/emission bands are noted with light grey stripes.

3.2.2. Mass Estimation

As shown by Afanasiev and Popović [25] and Afanasiev et al. [26], spectropolarimetric observations of galaxies with equatorial scattering make it possible to estimate the SMBH masses regardless of the inclination angle of the system to the observer. The radiation of the differentially rotating disc-shaped BLR is reflected from the equatorial scattering region so that the observer registers the specific features in broad lines in polarized light, in particular, the S-shaped profile of the polarization angle, which is a marker of Keplerian motion in the

disk. The change of the polarization angle along the broad line is related to the gas rotation velocity in BLR:

$$\log(V/c) = a - 0.5 \log[\tan(\Delta\varphi)], \quad (12)$$

where $\Delta\varphi$ is relative variations of the polarization angle (see Figure 4), and -0.5 coefficient is consistent with the assumption of BLR Keplerian motion. The parameter a is a function of M_{BH} and can be written as

$$a = 0.5 \log\left[\frac{GM_{\text{BH}} \cos^2(\theta)}{c^2 R_{\text{sc}}}\right], \quad (13)$$

where R_{sc} is the inner radius of the scattering region, and θ is the angle between the BLR and the scatterer plane. From the assumption of coplanarity, we assume $\theta = 0$, which contributes no more than $\sim 10\%$ uncertainty to the mass estimate. Then the SMBH mass can be expressed as follows:

$$\log(M_{\text{BH}}/M_{\odot}) \approx 10.25 + 2a + \log(R_{\text{sc}}) \quad (14)$$

In Equation (14), the parameter a is determined from observational data, while the size of the scattering region R_{sc} is determined by indirect methods. It is commonly assumed that R_{sc} characterizes the inner boundary of the gas-dust region (so-called dusty torus). Currently, two methods based on IR observations are used to determine the size of the torus: interferometry in the near-IR and mid-IR range [61] and IR reverberation mapping [62].

Lyu et al. [63] presented the results of the reverberation mapping of the dust region of the galaxy VII Zw 244 in WISE W1 ($\sim 3.4 \mu\text{m}$) and W2 ($\sim 4.5 \mu\text{m}$) bands. The IR radiation shows a delay of about 340–360 days relative to the optical emission, which indicates the size of the region emitting in the IR range. However, IR observational methods localize deep regions of the dusty torus, where the optical thickness is $\gg 1$, while equatorial scattering occurs in a region where the optical thickness is of the order of 1 and electron scattering dominates [64]. An alternative method has recently been proposed for determining the position of the equatorial scattering region based on the reverberation mapping in polarized broad lines [65]. As well as other reverberation methods, this approach requires a large amount of observational time, which is why it was still not applied to this galaxy. However, even the first result for the Mrk 6 galaxy obtained within the given approach showed that the measured R_{sc} turned out to be 2 times smaller than the size of the dusty torus estimated in the IR band. This case allows us to assume that for VII Zw 244 $R_{\text{sc}} \approx 170$ lt days.

Additionally, we are able to calculate the value of R_{sc} based on scale relation from [26]. According to this work, $R_{\text{sc}} \simeq 5.1 R_{\text{BLR}}$, where we take the estimate of the size of the area BLR R_{BLR} from Malygin et al. [30]: $R_{\text{BLR}} = 30.7^{+2.1}_{-2.3}$ lt days. Then $R_{\text{sc}} \simeq 157$ lt days. This value turns out to be approximately equal to half the size of the dust region in the IR range, and then we will use it to estimate the SMBH mass.

Since for VII Zw 244 the signs of equatorial scattering were detected in two broad lines, we present the profiles of the polarization angle switch for $\text{H}\alpha$ and $\text{H}\beta$ (Figure 4). The upper panels show variations of the polarization angle relative to the average level. In both lines, it can be seen that $\Delta\varphi$ to the right from the line center takes positive values; at the same time, the left negative wing of the profile is detected only in the $\text{H}\beta$ line. While the $\text{H}\alpha$ polarization angle profile is not symmetric as it is predicted by the model of the pure Keplerian motion, based on the sample provided in [26] one could find close examples of asymmetric polarization angle switch, as e.g., Mrk 1501 (see Figure 4 there). It can be assumed that the blue wing of the $\text{H}\alpha$ line profile suffers from depolarization, which may be associated with radial outflows from the region [66].

On the bottom panels of Figure 4 the dependence of the logarithm of the gas velocity in the line $\log(V/c)$ on the logarithm of the tangent of the polarization angle variations $\log[\tan(\Delta\varphi)]$ is presented. Regardless of the $\text{H}\alpha$ line profile asymmetry, the data points of

the measured values of the gas velocity $\log(V/c)$ show clearly the linear dependence on $\log[\tan(\Delta\phi)]$ in both emission lines, which is a significant proof of the observed Keplerian-like motion. Fitting the observed points by linear regression we estimated $a = -2.12 \pm 0.15$ for $H\beta$ and -2.05 ± 0.14 for $H\alpha$. In the case of both broad lines, the mass estimates turn out to be close: $\log(M_{\text{BH}}/M_{\odot}) = 8.21 \pm 0.29$ for $H\beta$ and 8.35 ± 0.29 for $H\alpha$. Note that if we assume $R_{\text{sc}} = 350$ lt days, as follows from the IR observations, then $\log(M_{\text{BH}}/M_{\odot}) \approx 8.6$, which is consistent with the estimate obtained above, within the error. Additionally, it is important to mention that the uncertainty obtained here was calculated as the variance of the deviation of the measured values of the gas velocity in the broad line from the Keplerian ones, which is assumed to be a random value distribution. As it can be seen in [26], 0.2–0.3 dex is a typical uncertainty for the spectropolarimetric mass measurements.

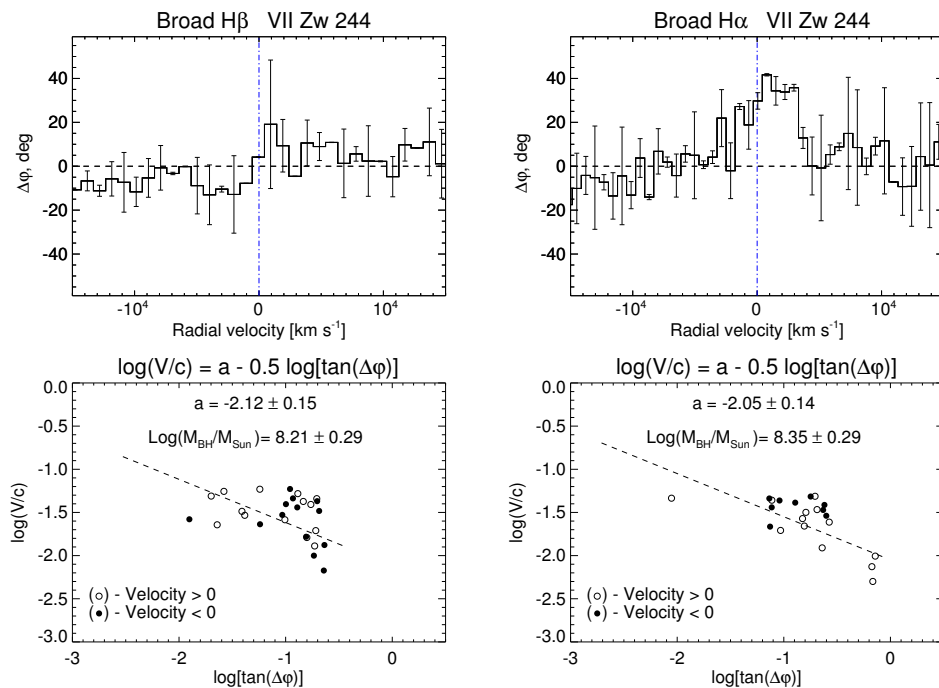


Figure 4. The polarization angle profiles for $H\beta$ (left) and $H\alpha$ (right) lines. On the upper panels the deviation of the polarization angle to the mean value (horizontal dashed line) is given. The bottom panels show the relation of $\log[\tan(\Delta\phi)]$ v.s. $\log(V/c)$.

3.2.3. Bolometric Luminosity

For this object we are also using results of our observations on BTA 6 m telescope $\log[L_{5100}(\text{erg/s})] = 44.22$ [30] and bolometric correction $BC = 10.3$. So $\log[L_{\text{bol}}(\text{erg/s})] = 45.24$. Note that in Lani et al. [67] a close value of $\log[L_{5100}(\text{erg/s})] = 44.16$ was obtained.

3.2.4. Inclination Angle and Spin Value

As shown in [26], the inclination angle of the AGN can be obtained by comparing two independent measurements of the SMBH mass. The estimate of the SMBH mass obtained from the reverberation mapping is known up to the dimensionless parameter f (see Equation (10)). In the paper by Malygin et al. [30] the obtained value of the SMBH mass is given for $f = 1$, so for VII Zw 244 $\log(V.P./M_{\odot}) = 7.05_{-0.08}^{+0.07}$. Comparing $V.P.$ with the mass estimate $\log(M_{\text{BH}}/M_{\odot}) = 8.3 \pm 0.3$ obtained from spectropolarimetric approach, we get $f = 21.1 \pm 10.1$. According to Yu et al. [68], the factor f is connected to kinematics, geometry and inclination of the BLR clouds and can be determined as $f = [h^2 + \sin^2(i)]^{-1}$, where h is

the ratio of the height to radius of the thick disk BLR (or the ratio of the turbulent velocity to the local Keplerian velocity for a given radius), which can be assumed $h = 0$ for geometrically thin disks. Then for VII Zw 244 the angle of inclination is $i = (14.3 \pm 3.6)^\circ$. Note here that although the average inclination angle of AGNs with equatorial scattering is $\sim 35^\circ$, objects with $i \sim 14^\circ$ have already been previously detected in the sample of AGNs with equatorial scattering, e.g., Mrk 1148 [26].

Using the same approach as for the previous one [53] and mass from Malygin et al. [30] we get that $i \gtrsim 18^\circ$. Moreover, Zhuang et al. [69] obtained the value $i \approx 15^\circ$ for this object independently by quantifying the contribution of the torus luminosity to the total IR emission. So, taking into account other estimates we concluded that in this case $i \approx 18^\circ$. As can be seen, this value agrees well with the independent estimates shown above obtained by IR SED analysis [69] and SMBH masses estimates comparison. The results of estimations of spin are presented in Table 2. $a \approx 0.996$ is a rather typical value for objects of this type.

In Hu et al. [70] the authors obtained close values of time lag (coinciding within the error limits). To calculate $V.P.$, they measured the velocity by σ_{line} (square root of the second moment) using the rms spectrum. The authors obtained values of the virial product that are smaller than in Malygin et al. [30], where the gas velocity was measured via the σ_{line} from the single epoch spectrum of a good signal-to-noise ratio with decomposition and subtraction of narrow components near the $H\beta$ line. Thus, the $V.P.$ from [70], compared with the spectropolarimetric mass measurement, gives an inclination angle of the system of about $\sim 11^\circ$, from which one can conclude that their measurement of the virial product is probably underestimated.

3.2.5. Magnetic Field

This object is radio quiet [71], however, according to recent studies [72–74], radio-quiet AGNs can have jets and emission mechanisms similar to radio-loud objects. Therefore, we decided that it would be useful to try to apply method from Piotrovich et al. [58] (Equation (11)) to this object as well. For this object we also take value ϑ_{line} from Malygin et al. [30] and calculate $FWHM = 2.335 \cdot \vartheta_{line}$ because in this case ϑ_{line} referred to $H\beta$ line.

This object has equatorial scattering, which does not allow us to consider the accretion disk as the only source of polarization. Thus, it is not possible to determine the magnetic field strength using the method from Piotrovich et al. [57].

The result is shown in Table 2. The obtained value of the magnetic field is also quite typical.

4. Conclusions

Here we presented the results of the spectropolarimetric observations of 2 type 1 AGNs from the reverberation mapping sample from [29]. The measured polarization properties have been used for exploring polarization mechanisms and the determination of physical parameters of the given AGN. We outline the following conclusions:

- for LEDA 3095839, no signs of equatorial scattering were detected in the polarized spectrum. At the same time, we estimated the level of continuous polarization as $(0.9 \pm 0.4)\%$, which is generated, as we believe, in an accretion disk. Using the approach from Du et al. [50] we came to the conclusion that for this object it makes sense to consider two options: inclination angle $i \approx 35^\circ$ and $i \approx 45^\circ$. Thus, we obtained spin values $a = 0.966^{+0.030}_{-0.106}$ and $a = 0.736^{+0.226}_{-0.368}$ and magnetic field strengths at event horizon of SMBH $\log(B_H[G]) = 4.06^{+0.24}_{-0.24}$ and $\log(B_H[G]) = 4.00^{+0.56}_{-0.34}$ respectively. Additionally, we estimated magnetic field strength and the exponent s of the power-law dependence of the magnetic field on the radius in accretion disk via polarimetric data using model from Piotrovich et al. [57] for this two cases: $\log(B_H^*[G]) = 3.53^{+0.26}_{-0.53}$, $s = 1.77 \pm 0.18$ and $\log(B_H^*[G]) = 4.08^{+0.30}_{-1.08}$, $s = 1.63 \pm 0.23$.

- for VII Zw 244 we detected the specific features of equatorial scattering in both H α and H β broad lines. It allowed us to estimate the SMBH mass as $\log(M_{\text{BH}}/M_{\odot}) = 8.3 \pm 0.3$. The comparison of the given mass with the previously obtained results gave the estimation of the inclination angle $i = (14.3 \pm 3.6)^{\circ}$, which allowed us to use the approach from Du et al. [50] (estimation via the AGN luminosity) assuming that $i \approx 18^{\circ}$ (minimum possible value for this object in this method). This approach give us the spin value $a = 0.996^{+0.002}_{-0.012}$ and magnetic field strength at event horizon of SMBH $\log(B_{\text{H}}[\text{G}]) = 4.29^{+0.10}_{-0.13}$.

Author Contributions: Conceptualization, M.P. and E.S.; methodology, M.P. and E.S.; software, M.P., E.S. and E.M.; validation, S.B. and T.N.; formal analysis, M.P.; investigation, M.P., E.S., E.M., S.B. and T.N.; resources, E.S. and E.M.; data curation, E.S. and E.M.; writing—original draft preparation, M.P., E.S. and E.M.; writing—review and editing, M.P., E.S. and E.M.; visualization, E.S. and E.M.; supervision, M.P. and E.S.; project administration, M.P. and E.S.; funding acquisition, E.S. All authors have read and agreed to the published version of the manuscript.

Funding: This work was supported by the Russian Scientific Foundation (grant no. 20-12-00030 “Investigation of geometry and kinematics of ionized gas in active galactic nuclei by polarimetry methods”).

Data Availability Statement: The data underlying this article are available in the article.

Acknowledgments: Observations with the SAO RAS telescopes are supported by the Ministry of Science and Higher Education of the Russian Federation. The renovation of telescope equipment is currently provided within the national project “Science and Universities”. The authors are grateful to the reviewers for useful comments.

Conflicts of Interest: The authors declare no conflict of interest.

Notes

- ¹ Details about the characteristics of medium-band filters can be found at https://www.sao.ru/hq/lsvfo/devices/scorpio-2/filters_eng.html Accessed 15 Jul. 2022.
- ² Details about the characteristics of gratings can be found at https://www.sao.ru/hq/lsvfo/devices/scorpio-2/grisms_eng.html Accessed 15 Jul. 2022.
- ³ The GAIA parallax of the star (2MASS J08540279+7700478) indicates it is located at the distance of 400 pc [40].

References

1. Kormendy, J.; Ho, L.C. Coevolution (Or Not) of Supermassive Black Holes and Host Galaxies. *ARA&A* **2013**, *51*, 511–653. <https://doi.org/10.1146/annurev-astro-082708-101811>.
2. Heckman, T.M.; Best, P.N. The Coevolution of Galaxies and Supermassive Black Holes: Insights from Surveys of the Contemporary Universe. *ARA&A* **2014**, *52*, 589–660. <https://doi.org/10.1146/annurev-astro-081913-035722>.
3. Daly, R.A. Estimates of black hole spin properties of 55 sources. *Mon. Not. R. Astron. Soc.* **2011**, *414*, 1253–1262. <https://doi.org/10.1111/j.1365-2966.2011.18452.x>.
4. Blandford, R.D.; Znajek, R.L. Electromagnetic extraction of energy from Kerr black holes. *Mon. Not. R. Astron. Soc.* **1977**, *179*, 433–456. <https://doi.org/10.1093/mnras/179.3.433>.
5. Blandford, R.D.; Payne, D.G. Hydromagnetic flows from accretion discs and the production of radio jets. *Mon. Not. R. Astron. Soc.* **1982**, *199*, 883–903. <https://doi.org/10.1093/mnras/199.4.883>.
6. Garofalo, D.; Evans, D.A.; Sambruna, R.M. The evolution of radio-loud active galactic nuclei as a function of black hole spin. *Mon. Not. R. Astron. Soc.* **2010**, *406*, 975–986. <https://doi.org/10.1111/j.1365-2966.2010.16797.x>.
7. Bardeen, J.M.; Press, W.H.; Teukolsky, S.A. Rotating Black Holes: Locally Nonrotating Frames, Energy Extraction, and Scalar Synchrotron Radiation. *Astrophys. J.* **1972**, *178*, 347–370. <https://doi.org/10.1086/151796>.
8. Novikov, I.D.; Thorne, K.S. Astrophysics of black holes. In *Black Holes (Les Astres Occlus)*; Dewitt, C.; Dewitt, B.S., Eds.; Gordon and Breach: New York, NY, USA, 1973; pp. 343–450.
9. Krolik, J.H. Making black holes visible: accretion, radiation, and jets. In Proceedings of the 2007 STScI Spring Symposium on Black Holes, Baltimore, MD, USA, 23–26 April 2007; pp. 309–321.
10. Krolik, J.H.; Hawley, J.F.; Hirose, S. The Relationship between Accretion Disks and Jets. *Rev. Mex. Astron. Astrofis. Conf. Ser.* **2007**, *27*, 1–7.
11. Martin, P.G.; Thompson, I.B.; Maza, J.; Angel, J.R.P. The polarization of Seyfert galaxies. *Astrophys. J.* **1983**, *266*, 470–478. <https://doi.org/10.1086/160795>.
12. Webb, W.; Malkan, M.; Schmidt, G.; Impey, C. The Wavelength Dependence of Polarization of Active Galaxies and Quasars. *Astrophys. J.* **1993**, *419*, 494. <https://doi.org/10.1086/173503>.
13. Impey, C.D.; Malkan, M.A.; Webb, W.; Petry, C.E. Ultraviolet Spectropolarimetry of High-Redshift Quasars with the Hubble Space Telescope. *Astrophys. J.* **1995**, *440*, 80. <https://doi.org/10.1086/175249>.
14. Wilkes, B.J.; Schmidt, G.D.; Smith, P.S.; Mathur, S.; McLeod, K.K. Optical Detection of the Hidden Nuclear Engine in NGC 4258. *ApJ* **1995**, *455*, L13. <https://doi.org/10.1086/309817>.

15. Barth, A.J.; Tran, H.D.; Brotherton, M.S.; Filippenko, A.V.; Ho, L.C.; van Breugel, W.; Antonucci, R.; Goodrich, R.W. Polarized Narrow-Line Emission from the Nucleus of NGC 4258. *Astron. J.* **1999**, *118*, 1609–1617. <https://doi.org/10.1086/301055>.
16. Smith, J.E.; Young, S.; Robinson, A.; Corbett, E.A.; Giannuzzo, M.E.; Axon, D.J.; Hough, J.H. A spectropolarimetric atlas of Seyfert 1 galaxies. *Mon. Not. R. Astron. Soc.* **2002**, *335*, 773–798 <https://doi.org/10.1046/j.1365-8711.2002.05665.x>.
17. Modjaz, M.; Moran, J.M.; Kondratko, P.T.; Greenhill, L.J. Probing the Magnetic Field at Subparsec Radii in the Accretion Disk of NGC 4258. *Astrophys. J.* **2005**, *626*, 104–119. <https://doi.org/10.1086/429559>.
18. Afanasiev, V.L.; Borisov, N.V.; Gnedin, Y.N.; Natsvlshvili, T.M.; Piotrovich, M.Y.; Buliga, S.D. Spectropolarimetric observations of active galactic nuclei with the 6-m BTA telescope. *Astron. Lett.* **2011**, *37*, 302–310. <https://doi.org/10.1134/S106377371105001X>.
19. Afanasiev, V.L.; Gnedin, Y.N.; Piotrovich, M.Y.; Natsvlshvili, T.M.; Buliga, S.D. Determination of Supermassive Black Hole Spins Based on the Standard Shakura-Sunyaev Accretion Disk Model and Polarimetric Observations. *Astron. Lett.* **2018**, *44*, 362–369. <https://doi.org/10.1134/S1063773718060014>.
20. Pariev, V.I.; Blackman, E.G.; Boldyrev, S.A. Extending the Shakura-Sunyaev approach to a strongly magnetized accretion disc model. *A&A* **2003**, *407*, 403–421. <https://doi.org/10.1051/0004-6361:20030868>.
21. Netzer, H.; Trakhtenbrot, B. Bolometric luminosity black hole growth time and slim accretion discs in active galactic nuclei. *Mon. Not. R. Astron. Soc.* **2014**, *438*, 672–679. <https://doi.org/10.1093/mnras/stt2238>.
22. Shakura, N.I.; Sunyaev, R.A. Black holes in binary systems. Observational appearance. *A&A* **1973**, *24*, 337–355.
23. Peterson, B.M. Measuring the Masses of Supermassive Black Holes. *Space Sci. Rev.* **2014**, *183*, 253–275. <https://doi.org/10.1007/s11214-013-9987-4>.
24. Blandford, R.D.; McKee, C.F. Reverberation mapping of the emission line regions of Seyfert galaxies and quasars. *Astrophys. J.* **1982**, *255*, 419–439. <https://doi.org/10.1086/159843>.
25. Afanasiev, V.L.; Popović, L.Č. Polarization in Lines—A New Method for Measuring Black Hole Masses in Active Galaxies. *ApJ* **2015**, *800*, L35. <https://doi.org/10.1088/2041-8205/800/2/L35>.
26. Afanasiev, V.L.; Popović, L.Č.; Shapovalova, A.I. Spectropolarimetry of Seyfert 1 galaxies with equatorial scattering: black hole masses and broad-line region characteristics. *Mon. Not. R. Astron. Soc.* **2019**, *482*, 4985–4999. <https://doi.org/10.1093/mnras/sty2995>.
27. Savić, Đ.V.; Popović, L.Č.; Shablovinskaya, E. The First Supermassive Black Hole Mass Measurement in Active Galactic Nuclei Using the Polarization of Broad Emission Line Mg II. *ApJ* **2021**, *921*, L21. <https://doi.org/10.3847/2041-8213/ac2d30>.
28. Bentz, M.C.; Denney, K.D.; Grier, C.J.; Barth, A.J.; Peterson, B.M.; Vestergaard, M.; Bennert, V.N.; Canalizo, G.; De Rosa, G.; Filippenko, A.V.; et al. The Low-luminosity End of the Radius-Luminosity Relationship for Active Galactic Nuclei. *Astrophys. J.* **2013**, *767*, 149. <https://doi.org/10.1088/0004-637X/767/2/149>.
29. Uklein, R.I.; Malygin, E.A.; Shablovinskaya, E.S.; Perepelitsyn, A.E.; Grokhovskaya, A.A. Photometric Reverberation Mapping of AGNs at $0.1 < z < 0.8$. I. Observational Technique. *Astrophys. Bull.* **2019**, *74*, 388–395. <https://doi.org/10.1134/S1990341319040059>.
30. Malygin, E.A.; Shablovinskaya, E.S.; Uklein, R.I.; Grokhovskaya, A.A. Measurement of the Supermassive Black Hole Masses in Two Active Galactic Nuclei by the Photometric Reverberation Mapping Method. *Astron. Lett.* **2020**, *46*, 726–733. <https://doi.org/10.1134/S1063773720110055>.
31. Afanasiev, V.L.; Moiseev, A.V. Scorpio on the 6 m Telescope: Current State and Perspectives for Spectroscopy of Galactic and Extragalactic Objects. *Balt. Astron.* **2011**, *20*, 363–370. <https://doi.org/10.1515/astro-2017-0305>.
32. Oliva, E. Wedged double Wollaston, a device for single shot polarimetric measurements. *A&AS* **1997**, *123*, 589–592. <https://doi.org/10.1051/aas:1997123589>.
33. Geyer, E.H.; Kiselev, N.N.; Chernova, G.P.; Jockers, K. Surface Polarimetry of Comet Tanaka-Machholz 1992d Using a Novel Double Wollaston Prism. In *Asteroids, Comets, Meteors*; LPI Contributions: Houston, TX, 1993; Volume 810, p. 116.
34. Afanasiev, V.L.; Amirkhanyan, V.R.; Moiseev, A.V.; Uklein, R.I.; Perepelitsyn, A.E. SCORPIO-2 guiding and calibration system in the prime focus of the 6-m telescope. *Astrophys. Bull.* **2017**, *72*, 458–468. <https://doi.org/10.1134/S1990341317040095>.
35. Popović, L.Č.; Afanasiev, V.L.; Shablovinskaya, E.S.; Ardilanov, V.I.; Savić, D. Spectroscopy and polarimetry of the gravitationally lensed quasar Q0957+561. *A&A* **2021**, *647*, A98. <https://doi.org/10.1051/0004-6361/202039914>.
36. Afanasiev, V.L.; Amirkhanyan, V.R. Technique of polarimetric observations of faint objects at the 6-m BTA telescope. *Astrophys. Bull.* **2012**, *67*, 438–452. <https://doi.org/10.1134/S1990341312040074>.
37. Shablovinskaya, E.S.; Afanasiev, V.L. The intraday variations of the polarization vector direction in radio source S5 0716+714. *Mon. Not. R. Astron. Soc.* **2019**, *482*, 4322–4328. <https://doi.org/10.1093/mnras/sty2943>.
38. Simmons, J.F.L.; Stewart, B.G. Point and interval estimation of the true unbiased degree of linear polarization in the presence of low signal-to-noise ratios. *A&A* **1985**, *142*, 100–106.
39. Press, W.H.; Teukolsky, S.A.; Vetterling, W.T.; Flannery, B.P. *Numerical Recipes 3rd Edition: The Art of Scientific Computing*; Cambridge University Press: Cambridge, UK, 2007.
40. Gaia Collaboration. VizieR Online Data Catalog: Gaia EDR3 (Gaia Collaboration, 2020). *VizieR Online Data Catalog* **2020**, p. I/350. <https://cdsarc.cds.unistra.fr/viz-bin/cat/I/350> Accessed 15 Jul. 2022.
41. Xu, Y.; Cao, X.W. Evidence of the Link between Broad Emission Line Regions and Accretion Disks in Active Galactic Nuclei. *Chin. J. Astron. Astrophys.* **2007**, *7*, 63–70. <https://doi.org/10.1088/1009-9271/7/1/03>.

42. Xu, D.W.; Komossa, S.; Wei, J.Y.; Qian, Y.; Zheng, X.Z. An Active Galactic Nucleus Sample with High X-Ray-to-Optical Flux Ratio from RASS. II. Optical Emission Line Properties of Seyfert 1-Type Active Galactic Nuclei. *Astrophys. J.* **2003**, *590*, 73–85. <https://doi.org/10.1086/374978>.
43. Richards, G.T.; Lacy, M.; Storrie-Lombardi, L.J.; Hall, P.B.; Gallagher, S.C.; Hines, D.C.; Fan, X.; Papovich, C.; Vanden Berk, D.E.; Trammell, G.B.; et al. Spectral Energy Distributions and Multiwavelength Selection of Type 1 Quasars. *Astrophys. J. Suppl. Ser.* **2006**, *166*, 470–497. <https://doi.org/10.1086/506525>.
44. Hopkins, P.F.; Richards, G.T.; Hernquist, L. An Observational Determination of the Bolometric Quasar Luminosity Function. *Astrophys. J.* **2007**, *654*, 731–753. <https://doi.org/10.1086/509629>.
45. Cheng, H.; Yuan, W.; Liu, H.Y.; Breeveld, A.A.; Jin, C.; Liu, B. Modelling accretion disc emission with generalized temperature profile and its effect on AGN spectral energy distribution. *Mon. Not. R. Astron. Soc.* **2019**, *487*, 3884–3903. <https://doi.org/10.1093/mnras/stz1532>.
46. Netzer, H. Bolometric correction factors for active galactic nuclei. *Mon. Not. R. Astron. Soc.* **2019**, *488*, 5185–5191. <https://doi.org/10.1093/mnras/stz2016>.
47. Duras, F.; Bongiorno, A.; Ricci, F.; Piconcelli, E.; Shankar, F.; Lusso, E.; Bianchi, S.; Fiore, F.; Maiolino, R.; Marconi, A.; et al. Universal bolometric corrections for active galactic nuclei over seven luminosity decades. *A&A* **2020**, *636*, A73. <https://doi.org/10.1051/0004-6361/201936817>.
48. Davis, S.W.; Laor, A. The Radiative Efficiency of Accretion Flows in Individual Active Galactic Nuclei. *Astrophys. J.* **2011**, *728*, 98. <https://doi.org/10.1088/0004-637X/728/2/98>.
49. Raimundo, S.I.; Fabian, A.C.; Vasudevan, R.V.; Gandhi, P.; Wu, J. Can we measure the accretion efficiency of active galactic nuclei? *Mon. Not. R. Astron. Soc.* **2012**, *419*, 2529–2544. <https://doi.org/10.1111/j.1365-2966.2011.19904.x>.
50. Du, P.; Hu, C.; Lu, K.X.; Wang, F.; Qiu, J.; Li, Y.R.; Bai, J.M.; Kaspi, S.; Netzer, H.; Wang, J.M.; et al. Supermassive Black Holes with High Accretion Rates in Active Galactic Nuclei. I. First Results from a New Reverberation Mapping Campaign. *Astrophys. J.* **2014**, *782*, 45. <https://doi.org/10.1088/0004-637X/782/1/45>.
51. Trakhtenbrot, B. The Most Massive Active Black Holes at $z \sim 1.5$ –3.5 have High Spins and Radiative Efficiencies. *Astrophys. J.* **2014**, *789*, L9. <https://doi.org/10.1088/2041-8205/789/1/L9>.
52. Lawther, D.; Vestergaard, M.; Raimundo, S.; Grupe, D. A catalogue of optical to X-ray spectral energy distributions of $z \approx 2$ quasars observed with Swift - I. First results. *Mon. Not. R. Astron. Soc.* **2017**, *467*, 4674–4710. <https://doi.org/10.1093/mnras/stx423>.
53. Piotrovich, M.Y.; Buliga, S.D.; Natsvlshvili, T.M. Determination of supermassive black hole spins in local active galactic nuclei. *Astron. Nachrichten* **2022**, *343*, e10020. <https://doi.org/10.1002/asna.20210020>.
54. Sobolev, V.V. *A Treatise on Radiative Transfer*; Van Nostrand: Princeton, NJ, USA, 1963.
55. Chandrasekhar, S. *Radiative Transfer*; Clarendon Press: Oxford, UK, 1950.
56. Gnedin, Y.N.; Piotrovich, M.Y.; Silant'ev, N.A.; Natsvlshvili, T.M.; Buliga, S.D. Polarization of Radiation and Basic Parameters of the Circumnuclear Region of Active Galactic Nuclei. *Astrophysics* **2015**, *58*, 443–452. <https://doi.org/10.1007/s10511-015-9398-1>.
57. Piotrovich, M.; Buliga, S.; Natsvlshvili, T. Determination of the Magnetic Field Strength and Geometry in the Accretion Disks of AGNs by Optical Spectropolarimetry. *Universe* **2021**, *7*, 202. <https://doi.org/10.3390/universe7060202>.
58. Piotrovich, M.Y.; Mikhailov, A.G.; Buliga, S.D.; Natsvlshvili, T.M. Determination of magnetic field strength on the event horizon of supermassive black holes in active galactic nuclei. *Mon. Not. R. Astron. Soc.* **2020**, *495*, 614–620. <https://doi.org/10.1093/mnras/staa1268>.
59. Daly, R.A. Black Hole Spin and Accretion Disk Magnetic Field Strength Estimates for More Than 750 Active Galactic Nuclei and Multiple Galactic Black Holes. *Astrophys. J.* **2019**, *886*, 37. <https://doi.org/10.3847/1538-4357/ab35e6>.
60. Smith, J.E.; Robinson, A.; Young, S.; Axon, D.J.; Corbett, E.A. Equatorial scattering and the structure of the broad-line region in Seyfert nuclei: evidence for a rotating disc. *Mon. Not. R. Astron. Soc.* **2005**, *359*, 846–864. <https://doi.org/10.1111/j.1365-2966.2005.08895.x>.
61. Gravity Collaboration.; Pfuhl, O.; Davies, R.; Dexter, J.; Netzer, H.; Hönig, S.; Lutz, D.; Schartmann, M.; Sturm, E.; Amorim, A.; et al. An image of the dust sublimation region in the nucleus of NGC 1068. *A&A* **2020**, *634*, A1. <https://doi.org/10.1051/0004-6361/201936255>.
62. Yang, Q.; Shen, Y.; Liu, X.; Agüena, M.; Annis, J.; Avila, S.; Banerji, M.; Bertin, E.; Brooks, D.; Burke, D.; et al. Dust Reverberation Mapping in Distant Quasars from Optical and Mid-infrared Imaging Surveys. *Astrophys. J.* **2020**, *900*, 58. <https://doi.org/10.3847/1538-4357/aba59b>.
63. Lyu, J.; Rieke, G.H.; Smith, P.S. Mid-IR Variability and Dust Reverberation Mapping of Low- z Quasars. I. Data, Methods, and Basic Results. *Astrophys. J.* **2019**, *886*, 33. <https://doi.org/10.3847/1538-4357/ab481d>.
64. Savić, D.; Goosmann, R.; Popović, L.Č.; Marin, F.; Afanasiev, V.L. AGN black hole mass estimates using polarization in broad emission lines. *A&A* **2018**, *614*, A120. <https://doi.org/10.1051/0004-6361/201732220>.
65. Shablovinskaya, E.S.; Afanasiev, V.L.; Popović, L.Č. Measuring the AGN Sublimation Radius with a New Approach: Reverberation Mapping of Broad Line Polarization. *Astrophys. J.* **2020**, *892*, 118. <https://doi.org/10.3847/1538-4357/ab7849>.

66. Savić, Đ.; Popović, L.Č.; Shablovinskaya, E.; Afanasiev, V.L. Estimating supermassive black hole masses in active galactic nuclei using polarization of broad Mg II, H α , and H β lines. *Mon. Not. R. Astron. Soc.* **2020**, *497*, 3047–3054. <https://doi.org/10.1093/mnras/staa2039>.
67. Lani, C.; Netzer, H.; Lutz, D. Intrinsic AGN SED & black hole growth in the Palomar-Green quasars. *Mon. Not. R. Astron. Soc.* **2017**, *471*, 59–79. <https://doi.org/10.1093/mnras/stx1374>.
68. Yu, L.M.; Bian, W.H.; Wang, C.; Zhao, B.X.; Ge, X. Calibration of the virial factor f in supermassive black hole masses of reverberation-mapped AGNs. *Mon. Not. R. Astron. Soc.* **2019**, *488*, 1519–1534. <https://doi.org/10.1093/mnras/stz1766>.
69. Zhuang, M.Y.; Ho, L.C.; Shangguan, J. The Infrared Emission and Opening Angle of the Torus in Quasars. *Astrophys. J.* **2018**, *862*, 118. <https://doi.org/10.3847/1538-4357/aacc2d>.
70. Hu, C.; Li, S.S.; Yang, S.; Yang, Z.X.; Guo, W.J.; Bao, D.W.; Jiang, B.W.; Du, P.; Li, Y.R.; Xiao, M.; et al. Supermassive Black Holes with High Accretion Rates in Active Galactic Nuclei. XII. Reverberation Mapping Results for 15 PG Quasars from a Long-duration High-cadence Campaign. *Astrophys. J. Suppl. Ser.* **2021**, *253*, 20. <https://doi.org/10.3847/1538-4365/abd774>.
71. Laor, A.; Behar, E. On the origin of radio emission in radio-quiet quasars. *Mon. Not. R. Astron. Soc.* **2008**, *390*, 847–862. <https://doi.org/10.1111/j.1365-2966.2008.13806.x>.
72. Berton, M.; Järvelä, E.; Crepaldi, L.; Lähteenmäki, A.; Tornikoski, M.; Congiu, E.; Kharb, P.; Terreran, G.; Vietri, A. Absorbed relativistic jets in radio-quiet narrow-line Seyfert 1 galaxies. *A&A* **2020**, *636*, A64. <https://doi.org/10.1051/0004-6361/202037793>.
73. Silpa, S.; Kharb, P. Looking at Radio-Quiet AGN with Radio Polarimetry. *arXiv* **2022**, arXiv:2201.03877.
74. Hartley, P.; Jackson, N.; Sluse, D.; Stacey, H.R.; Vives-Arias, H. Strong lensing reveals jets in a sub-microJy radio-quiet quasar. *Mon. Not. R. Astron. Soc.* **2019**, *485*, 3009–3023. <https://doi.org/10.1093/mnras/stz510>.